

This discussion paper is/has been under review for the journal Climate of the Past (CP). Please refer to the corresponding final paper in CP if available.

# The Middle Miocene climate as modelled in an atmosphere-ocean-biosphere model

M. Krapp<sup>1,2</sup> and J. H. Jungclaus<sup>1</sup>

<sup>1</sup>Max-Planck Institut für Meteorologie, Hamburg, Germany

<sup>2</sup>International Max Planck Research School on Earth System Modelling, Hamburg, Germany

Received: 30 May 2011 – Accepted: 31 May 2011 – Published: 17 June 2011

Correspondence to: M. Krapp (mario.krapp@zmaw.de)

Published by Copernicus Publications on behalf of the European Geosciences Union.

CPD

7, 1935–1972, 2011

## The Middle Miocene climate

M. Krapp and  
J. H. Jungclaus

Title Page

Abstract

Introduction

Conclusions

References

Tables

Figures

◀

▶

◀

▶

Back

Close

Full Screen / Esc

Printer-friendly Version

Interactive Discussion



## Abstract

We present simulations with a coupled ocean-atmosphere-biosphere model for the Middle Miocene 15 million years ago. The Middle Miocene topography, which alters both large-scale ocean and atmospheric circulations, causes a global warming of 0.7 K compared to present-day. Higher than present-day CO<sub>2</sub> levels of 480 and 720 ppm cause a global warming of 2.8 and 4.9 K, thereby matching proxy-based Middle Miocene global temperature estimates of 3–6 K warming. Higher CO<sub>2</sub> levels and the associated water vapour feedback enhance the greenhouse effect and lead to a polar amplification of the warming. Although oceanic and atmospheric poleward heat transport are individually altered by 10–30 % in the mid and high latitudes, changes of the total heat transport account only for 4–8 %, pointing toward a compensation between oceanic and atmospheric heat transport. Our model reproduces a denser vegetation in agreement with fossil records. These results suggest that higher than present-day CO<sub>2</sub> levels are essential to drive the warm Middle Miocene climate.

## 15 1 Introduction

The warm climate of the Middle Miocene was the warmest period of the last 25 million years, contrasting the Cenozoic long term cooling (Zachos et al., 2001). Temperatures during the Middle Miocene were about 3–6 K warmer than today (Tripati et al., 2009). The equator-to-pole temperature gradient was reduced both over land and 20 ocean (Nikolaev, 2006; Bruch et al., 2007). The climate in Europe was warmer and more humid (Böhme et al., 2011; Bruch et al., 2010). Even in the Sahara region, conditions were wet to very wet, signalling less desert coverage (Senut et al., 2009). The continents were densely wooded; evergreen forests expanded to at least 45° N, and boreal forest expanded northward as far as the Arctic circle (Wolfe, 1985; Williams et al., 2008).

## The Middle Miocene climate

M. Krapp and  
J. H. Jungclaus

[Title Page](#)

[Abstract](#)

[Introduction](#)

[Conclusions](#)

[References](#)

[Tables](#)

[Figures](#)

◀

▶

◀

▶

[Back](#)

[Close](#)

[Full Screen / Esc](#)

[Printer-friendly Version](#)

[Interactive Discussion](#)



Reconstructions for atmospheric CO<sub>2</sub> levels estimate values between 180 ppm up to 550 ppm (Pagani et al., 1999; Royer et al., 2001; Kürschner et al., 2008). Translated into radiative forcing, the uncertainty accounts for about 2.6 W m<sup>-2</sup> for the direct effect of CO<sub>2</sub> only (Myhre et al., 1998). In a recent model study, the possible range of atmospheric CO<sub>2</sub> levels for the Middle Miocene was suggested to be between 460 and 580 ppm (You et al., 2009).

Previous modelling studies for the Middle Miocene used atmosphere general circulation models (GCMs) with either prescribed sea surface temperatures or a mixed-layer ocean (You et al., 2009; Tong et al., 2009; Henrot et al., 2010; Herold et al., 2010). These models were able to reproduce the proxy-based global warming of 3–6 K, but they could not reproduce the flatter equator-to-pole temperature gradient. What all previous modelling studies have in common is that they lack the dynamics of an ocean GCM. Atmospheric GCMs can take into account tectonic changes such as mountain uplift, but they cannot account for oceanic gateway reconfigurations. For the last 25 million years, when atmospheric CO<sub>2</sub> was relatively low, both mountain uplift and oceanic gateway reconfigurations may have triggered large-scale shifts in climate (Zachos et al., 2001).

For our study, we use a fully coupled atmosphere-ocean-biosphere GCM to test if the results with the full ocean dynamics are consistent with previous modelling studies, and if we can improve the meridional temperature gradient mismatch. We perform a series of experiments to investigate (1) how topography and ocean gateways contribute to a warm Middle Miocene climate and (2) how higher than present-day CO<sub>2</sub> levels contribute to a warm Middle Miocene climate.

This paper is organised as follows. Section 2 describes the setup of our GCM and the experimental design. In Sect. 3, we present our experimental results and compare them to marine and terrestrial temperature reconstructions. Section 4 gives a summary and a discussion on our main findings. We conclude in Sect. 5.

## The Middle Miocene climate

M. Krapp and  
J. H. Jungclaus

[Title Page](#)

[Abstract](#)

[Introduction](#)

[Conclusions](#)

[References](#)

[Tables](#)

[Figures](#)

◀

▶

◀

▶

[Back](#)

[Close](#)

[Full Screen / Esc](#)

[Printer-friendly Version](#)

[Interactive Discussion](#)



## 2 Model set-up and experimental design

We use the atmosphere-ocean-biosphere general circulation model MPI-ESM. MPI-ESM is a comprehensive Earth-System Model that has been developed at the Max-Planck Institute for Meteorology in Hamburg. The dynamical core of the atmosphere model ECHAM5 is formulated in spherical harmonics (Roeckner et al., 2003). We use ECHAM5 in a T42 truncation, which corresponds to a horizontal grid spacing of  $2.8^\circ$ . ECHAM5 has 19 levels in the vertical, the uppermost being at 10 hPa. ECHAM5 incorporates the land surface model JSBACH that includes a dynamic vegetation module (Raddatz et al., 2007; Brovkin et al., 2009). The ocean model MPI-OM (Marsland et al., 2003) uses a tripolar curvilinear grid with a quasi-homogeneous horizontal grid spacing of about  $1^\circ$ . MPI-OM has 40 levels in the vertical, which are unequally spaced. The upper 150 m are resolved within ten levels. MPI-OM incorporates a dynamic-thermodynamic sea-ice model that follows the descriptions of Hibler and Semtner (Hibler, 1979; Semtner, 1976). MPI-OM and ECHAM5 exchange momentum flux, heat flux, and freshwater flux, as well as sea surface temperatures, sea-ice thickness, sea-ice fraction, and snow cover on sea-ice once per day via OASIS (Valcke, 2006).

The first two experiments differ in their applied topography (Fig. 1). The palaeotopography is based on a global plate rotation model, and the palaeobathymetry is reconstructed using an age-depth relationship for the oceanic crust with overlaid sediment thicknesses (Herold et al., 2008). Uncertainties for this reconstructed topography are largest in the mountain regions of Andes, Rocky Mountains, and the Tibetan Plateau. Furthermore, the seafloor is relatively smooth compared to present-day due to the lack of geological data (for details, see Herold et al., 2008). In contrast to present-day, several open ocean gateways connect the major ocean basins, for example, the open Panama Seaway, the Tethys, and a wider Indonesian Through-flow. The atmospheric circulation is affected by the topography as well, because large mountain regions like the Andes, the Himalayas, the Rocky Mountains, and the Alps are lower compared to present-day. We remove the Greenland Ice Sheet in all Middle Miocene experiments,

CPD

7, 1935–1972, 2011

## The Middle Miocene climate

M. Krapp and  
J. H. Jungclaus

[Title Page](#)

[Abstract](#)

[Introduction](#)

[Conclusions](#)

[References](#)

[Tables](#)

[Figures](#)

◀

▶

◀

▶

[Back](#)

[Close](#)

[Full Screen / Esc](#)

[Printer-friendly Version](#)

[Interactive Discussion](#)



because glaciation on Greenland had started later during the Pliocene (Raymo, 1994). We refer to the experiment with the Middle Miocene topography as MIOC360 and to the experiment with present-day topography as CTRL. In both CTRL and MIOC360 we prescribe present-day CO<sub>2</sub> levels of 360 ppm.

We decide to perform a present-day control simulation for two reasons. First of all, the climate can be easily validated against observation and re-analysis data, respectively. The root mean square errors (RMSE) for temperature, geopotential height, and sea level pressure with respect to ERA-40 re-analysis data (Uppala et al., 2005) are shown in Table 1. Compared to a stand-alone version of ECHAM5, that is forced with sea surface temperatures, the RMSEs in CTRL are larger. CTRL is based on the fully coupled MPI-ESM that includes an ocean and a vegetation model. Because of this increased complexity, the sources for errors might increase. Second, You et al. (2009) and Tong et al. (2009) already showed, that atmospheric CO<sub>2</sub> levels for the Middle Miocene can be constrained to higher than pre-industrial values.

In the last two experiments we assess the uncertainties of atmospheric CO<sub>2</sub> and prescribe higher than modern atmospheric CO<sub>2</sub> levels for the Middle Miocene. The experiment, where we prescribe a CO<sub>2</sub> level of 480 ppm, will be referred to as MIOC480. The experiment, where we prescribe a CO<sub>2</sub> level of 720 ppm, will be referred to as MIOC720. All experiments share the same present-day concentration of methane (650 ppb) and nitrous oxide (270 ppb). Orbital parameters are also kept at their present-day values.

CTRL is integrated for 2100 yr to reach quasi-equilibrium, MIOC360 for 2300 yr. Based on MIOC360, MIOC720 is then integrated for 2000 yr. After this integration we decrease the CO<sub>2</sub> level to 480 ppm and run the simulation for another 1000 yr to reach equilibrium in MIOC480. For the following analysis we use the last 100 yr of each experiment.

## The Middle Miocene climate

M. Krapp and  
J. H. Jungclaus

[Title Page](#)

[Abstract](#)

[Introduction](#)

[Conclusions](#)

[References](#)

[Tables](#)

[Figures](#)

◀

▶

◀

▶

[Back](#)

[Close](#)

[Full Screen / Esc](#)

[Printer-friendly Version](#)

[Interactive Discussion](#)



### 3 Results

The Middle Miocene topography allows for a large-scale reorganisation of both atmosphere and ocean circulation. Mountain regions affect the atmosphere, ocean gateways and bottom topography affect the ocean. Higher than present-day CO<sub>2</sub> affects the radiation balance, because CO<sub>2</sub> effectively absorbs long-wave radiation. We analyse the feedbacks of higher CO<sub>2</sub> on surface temperature using a simple, one-dimensional energy balance model. CO<sub>2</sub> alters surface temperatures as well as the hydrological cycle, both being factors that determine the vegetation.

In the following, we compare our results to previous model studies for the Middle Miocene. We, therefore, shortly describe the setups of these previous experiments keeping the original labels. You et al. (2009) performed atmospheric GCM experiments in which they prescribed a medium (SM) and a high (SH) meridional sea surface temperature gradient. In each of these SM and SH experiments atmospheric CO<sub>2</sub> was prescribed with 350 ppm (SM\_350 and SH\_350) and 700 ppm (SM\_700 and SM\_350). Tong et al. (2009) performed atmospheric GCM experiments coupled to a slab ocean with prescribed atmospheric CO<sub>2</sub> of 355 ppm (MidCO<sub>2</sub>) and 700 ppm (HighCO<sub>2</sub>). Henrot et al. (2010) performed an atmospheric GCM experiment (MM4-veg) in which CO<sub>2</sub> was prescribed to 500 ppm and in which a modelled Middle Miocene vegetation was taken into account.

#### 20 3.1 The role of topography

The global annual mean temperature in MIOC360 is 15.0 °C, being 0.7 K higher compared to 14.3 °C in CTRL (Table 2). Changes in the surface topography do not affect the ocean surface, but the continents. On average the global mean land surface temperature in MIOC360 is 1.2 K larger than in CTRL. Compared to a previous model study of You et al. (2009), the global annual mean temperature is 1.2–2.0 K colder (Table 3).

On a regional scale the warming in MIOC360 can be as large as 15 K, for example over Greenland (Fig. 3a). Because of the topographic changes, the continents are more affected than the ocean. A polar amplification leads to an enhanced warming

CPD

7, 1935–1972, 2011

## The Middle Miocene climate

M. Krapp and  
J. H. Jungclaus

[Title Page](#)

[Abstract](#)

[Introduction](#)

[Conclusions](#)

[References](#)

[Tables](#)

[Figures](#)

◀

▶

◀

▶

[Back](#)

[Close](#)

[Full Screen / Esc](#)

[Printer-friendly Version](#)

[Interactive Discussion](#)



## The Middle Miocene climate

M. Krapp and  
J. H. Jungclaus

[Title Page](#)

[Abstract](#)

[Introduction](#)

[Conclusions](#)

[References](#)

[Tables](#)

[Figures](#)

◀

▶

◀

▶

[Back](#)

[Close](#)

[Full Screen / Esc](#)

[Printer-friendly Version](#)

[Interactive Discussion](#)



of the high latitudes (Fig. 2a). Because of the summer sea-ice loss, less radiation is reflected back to space (Table 2). This ice-albedo feedback amplifies the high latitude warming.

We estimate the direct effect of the topography by the difference between the surface temperature and the potential temperature at 1000 hPa, which is near sea level pressure. The Middle Miocene land elevation in Fig. 1 is on average 644 m, which is 151 m lower compared to the present-day. On a global scale, the direct effect of the lower topography contributes 0.2 K to the global warming. The differences are large over regions where the Middle Miocene elevation is much lower than today, for example over Greenland (up to 15 K), over Antarctica (2 to 4 K), or over the South African plateau (up to 7 K).

Lower and displaced mountain regions deflect low level winds, for example over Greenland, Asia, or Western North America (Fig. 5). Winter storms, defined as deviations of the 2.5–6 days bandpass-filtered 500 hPa geopotential height (Blackmon, 1976), intensify over the North Pacific (Fig. 6b). The storms penetrate more inland, because the elevation of the Rocky Mountains is lower. As a consequence of the deflected low level winds, precipitation patterns shift (Fig. 4a). Over Eurasia, rainfall increases, while it decreases over Africa and over the Americas. The increase over Europe is in agreement with reconstructions of the mean annual precipitation (Bruch et al., 2010). Over the equatorial Pacific, precipitation decreases between 10° S and 10° N, but increases poleward of 10° S/N. The overall decrease over the Southern Hemisphere is mainly due to a reduction in convective precipitation (Fig. 2b). Despite these precipitation shifts, the global annual mean precipitation changes little (Table 2).

The ocean circulation is affected for three reasons. In the following, let us focus on the Atlantic Ocean. First, the horizontal circulation changes due to open ocean gateways and changes in surface winds. The subtropical gyre is weaker compared to CTRL, while the subpolar gyre is stronger (Fig. 7a, b). A westward flow through the Tethys establishes. This flow moves water from the Indian Ocean into the Atlantic and, thereby, contributes to a stronger northern cell in the equatorial current system. The

## The Middle Miocene climate

M. Krapp and  
J. H. Jungclaus

[Title Page](#)

[Abstract](#)

[Introduction](#)

[Conclusions](#)

[References](#)

[Tables](#)

[Figures](#)

◀

▶

◀

▶

[Back](#)

[Close](#)

[Full Screen / Esc](#)

[Printer-friendly Version](#)

[Interactive Discussion](#)



stronger cell dominates and suppresses the southern cell. Its remains are restricted to a weak western boundary current.

Second, the lateral flow through open ocean gateways changes the water mass properties of the adjacent oceans. Besides the eastern inflow of Indian Ocean water,

5 Pacific Ocean water enters the Atlantic Ocean through the Panama Seaway. These connections allow for a large-scale mixing between the oceans and, therefore, affect the water mass composition of the oceans (Fig. 8). Through the Panama Seaway, Atlantic deepwater enters the Pacific; Pacific deepwater becomes saltier and denser.

At the surface, however, the salinity contrast between Pacific and Atlantic increases.

10 This is contrary to other studies with an open Panama Seaway, where the salinity contrast is reduced and, therefore, leads to a weaker Atlantic meridional overturning circulation (AMOC) (Maier-Reimer et al., 1990; Lunt et al., 2007). Instead, the AMOC in MIOC360 is as strong as in CTRL (Fig. 9a, b). The mixing due to the eastern inflow

15 of Indian Ocean water through the Strait of Gibraltar is well reflected in the composition of Tethys water; it is located between the water masses of Atlantic and Indian Ocean.

Tethys water originates from the Indian Ocean. Along the way into the Atlantic, surface water evaporates and becomes denser than its original Indian Ocean source. Because the Tethys is no enclosed basin like the Mediterranean, the deep outflow water is not as dense as in CTRL.

20 Third, the ocean bathymetry affects deepwater formation. Because of the subsided Greenland-Scotland Ridge, the AMOC in MIOC360 extends more northward than in CTRL (Fig. 9a, b). Even at 80° N more than 4 Sv of Atlantic ocean water is converted into deep water.

The changes of the large-scale circulation in both atmosphere and ocean give rise

25 to a redistribution of heat, especially from low to high latitudes. The southward oceanic heat transport is enhanced by about 0.3 PW between 30° S and 45° S, while the northward heat transport is less enhanced (blue line in Fig. 10b). Though, changes in oceanic heat transport are compensated by the atmospheric heat transport and vice versa, leaving the total heat transport nearly unchanged (Fig. 10c, d).

### 3.2 The role of higher CO<sub>2</sub> levels

The CO<sub>2</sub> induced warming in MIOC480 and MIOC720 is more homogeneous than the localised topographic effects (Fig. 3b, c). Global annual mean temperatures in MIOC480 and MIOC720 are 17.1 °C and 19.2 °C, corresponding to an increase of 2.8 K and 4.9 K compared to CTRL (Table 2). Compared to previous model studies, both MIOC480 and MIOC720 are generally warmer (Table 3). Only SH\_700 (You et al., 2009) matches the surface temperature of 19.2 °C in MIOC720. The climate sensitivity in our study is 4.0 K (from 360 ppm to 720 ppm). This value is larger than 2.0 K in You et al. (2009) and 2.3 K in Tong et al. (2009).

The warming is more pronounced over the continents and at the high latitudes. Here, the warming causes a further retreat of sea ice (Table 2). In MIOC720, summer sea ice vanishes everywhere, except in some coastal areas. The further reduction in sea ice, again, amplifies the high latitude warming. Reconstructions also suggest that perennial Arctic sea ice develops after the warm Middle Miocene at about 13 Ma (Krylov et al., 2008). Because our CO<sub>2</sub> scenarios are warmer than previous studies, the sea-ice retreat under CO<sub>2</sub> forcing is also larger. We find a reduction of Northern Hemisphere winter sea ice that is three times as large (about 30 % from MIOC360 to MIOC720) as found by Tong et al. (about 10 % from MidCO<sub>2</sub> to HighCO<sub>2</sub>).

According to the Clausius-Clapeyron relation, a warmer atmosphere can hold more water. The atmospheric water vapour content is, therefore, largest in MIOC480 and MIOC720 (Fig. 2d, Table 2). The hydrological cycle enhances; the annual mean precipitation in MIOC480 and MIOC720 increases by 21 and 49 mm a<sup>-1</sup> compared to CTRL (Fig. 4b, c). Despite the enhanced hydrological cycle, cloud cover is reduced, mainly over the tropics (Fig. 2c). Precipitation in MIOC480 and MIOC720 is larger than in MidCO<sub>2</sub> or HighCO<sub>2</sub> (Tong et al., 2009), but is in good agreement with MM4-veg (Hernot et al., 2010). MM4-veg and MIOC480 deviate by less than one standard deviation.

The atmospheric circulation in MIOC480 remains generally unaltered compared to MIOC360 (Fig. 5b). Only in MIOC720, the circulation changes, mainly over the ocean

CPD

7, 1935–1972, 2011

## The Middle Miocene climate

M. Krapp and  
J. H. Jungclaus

[Title Page](#)

[Abstract](#)

[Introduction](#)

[Conclusions](#)

[References](#)

[Tables](#)

[Figures](#)

◀

▶

◀

▶

[Back](#)

[Close](#)

[Full Screen / Esc](#)

[Printer-friendly Version](#)

[Interactive Discussion](#)



## The Middle Miocene climate

M. Krapp and  
J. H. Jungclaus

[Title Page](#)

[Abstract](#)

[Introduction](#)

[Conclusions](#)

[References](#)

[Tables](#)

[Figures](#)

◀

▶

◀

▶

[Back](#)

[Close](#)

[Full Screen / Esc](#)

[Printer-friendly Version](#)

[Interactive Discussion](#)

(Fig. 5c). Over the Western Pacific, the trades are stronger, while they are weaker over the Eastern Pacific. Over the North Pacific, the low level winds increase. Winter storms intensify and they penetrate farther into Europe (Fig. 6d).

The ocean circulation in MIOC480 differs little from MIOC360 (Figs. 7c, 9b). As for the atmospheric circulation, only in MIOC720, the large-scale ocean circulation changes. A slow-down of the AMOC reduces the northward heat transport in the Atlantic Ocean (Fig. 9c and red dashed line in Fig. 10a). Here, the temperatures are lower compared to MIOC480, because less warm surface water is moved northward (Fig. 3c). As a result, the oceanic heat transport in the Northern Hemisphere becomes smaller (Fig. 10b). In turn, the atmospheric heat transport increases and compensates for the smaller oceanic heat transport. A detailed analysis on how the ocean gateways and the ocean bottom topography, for example the presence of the Greenland-Scotland Ridge, affect the stability of the AMOC, is subject of an ongoing sensitivity study.

We now apply a simple one-dimensional energy balance model (EBM) to quantitatively analyse the causes for the temperature differences, following the approach of Heinemann et al. (2009). In radiative equilibrium Earth's surface temperature  $T_{\text{surf}}$  is determined by the long-wave emissivity  $\varepsilon$ , the planetary albedo  $\alpha$ , and the meridional heat flux divergence  $H$  via the energy balance

$$I(\phi)[1 - \alpha(\phi)] - H(\phi) = \varepsilon(\phi)\sigma T_{\text{surf}}^4(\phi). \quad (1)$$

$\phi$  is the latitude,  $I$  is the latitudinal varying incoming solar radiation, and  $\sigma$  is the Stefan-Boltzmann constant. For reasons of readability we omit the latitude coordinate  $\phi$  in the following. We can diagnose the EBM parameters  $\alpha$ ,  $H$ , or  $\varepsilon$  from our GCM results to obtain the surface temperature according to Eq. (1). The zonally averaged temperature changes can then be contributed to one of  $\alpha$ ,  $H$ , or  $\varepsilon$ , while keeping the other two fixed. The difference between the surface temperature calculated by Eq. (1) and the surface temperature calculated by the GCM is only marginal; mean deviations are smaller than 0.25 K.



The reduced cloud cover over the tropics reduces the planetary albedo that, in turn, leads to enhanced warming in MIOC480 and MIOC720 (Fig. 11b, c). The increased export of heat effectively cools the tropics. The temperature change induced by the heat flux divergence  $H$  is, therefore, negative.

5 Long-wave emissivity  $\varepsilon$  largely contributes to the CO<sub>2</sub> induced warming in MIOC480 and MIOC720. The reduction of  $\varepsilon$  is in line with the increased water vapour content of the atmosphere (Table 2). The atmosphere in MIOC480 and MIOC720 contains 15 % and 30 % more water vapour than in MIOC360. Water vapour is an important greenhouse gas, because of its ability to absorb long-wave radiation. A decreased 10 long-wave emissivity  $\varepsilon$  in MIOC480 and MIOC720 simply means that the greenhouse effect is stronger.

The important factors that determine the vegetation cover are radiation, precipitation, and atmospheric CO<sub>2</sub>. Changes in these climate parameters evoke responses of the vegetation cover that affect the climate system in terms of surface albedo, roughness 15 length, moisture and heat fluxes, or runoff. In our experimental setups we intentionally change the topography and prescribe higher than present atmospheric CO<sub>2</sub> levels. While the topography changes the local radiation balance and shifts precipitation patterns, CO<sub>2</sub> can be accounted for changes in the hydrological cycle and a stronger greenhouse effect.

20 Vegetation starts to occupy regions where the land ice has been removed, for example over Greenland (Fig. 12b). High-latitude warming and higher CO<sub>2</sub> levels support a northward expansion of boreal forests. In MIOC480 and MIOC720, global forest cover is largest (Table 2, Fig. 12c, d). The large forest cover and the northward extension of forest is in line with vegetation reconstructions (Wolfe, 1985). Unfortunately, the 25 vegetation module in JSBACH cannot account for changes in soil properties, like field capacity or background albedo. They have to be prescribed with present-day values. Especially in today's extreme regions like the Sahara, vegetation growth is, therefore, restricted or inhibited. Desertification of the Sahara is assumed to have started later during the late Miocene 8–7 Ma ago (Senut et al., 2009). Although the high latitudes

## The Middle Miocene climate

M. Krapp and  
J. H. Jungclaus

[Title Page](#)

[Abstract](#)

[Introduction](#)

[Conclusions](#)

[References](#)

[Tables](#)

[Figures](#)

◀

▶

◀

▶

[Back](#)

[Close](#)

[Full Screen / Esc](#)

[Printer-friendly Version](#)

[Interactive Discussion](#)



are more densely wooded in MIOC720 than in MIOC480, average low latitude temperatures of more than 30 °C lead to a retreat of tropical rainforest. On its expense, deserts expand. The global desert cover has, therefore, a minimum in MIOC480 (Table 2).

### 3.3 Comparison to proxy data

- 5 We compare the modelled palaeo temperatures to proxy based reconstructions for the Middle Miocene. We use terrestrial reconstructions to evaluate land surface temperatures and marine reconstructions to evaluate sea surface temperatures. The sites of the marine proxies are spread all over the oceans, while terrestrial proxies are mainly recovered from the Northern Hemisphere, especially over Europe, East Asia and the  
10 coasts of North America (Fig. 13a).

#### 3.3.1 Terrestrial Proxies

Terrestrial climate reconstructions based on the coexistence approach estimate the lower and the upper mean annual temperature from plant fossils (Mosbrugger and Utescher, 1997). We use terrestrial temperature data from the 2010 NECLIME data set (Utescher et al., 2011). The data set is also available from PANGAEA, <http://www.pangaea.de>. We compare reconstructed land surface temperatures obtained from the coexistence approach to our modelled land surface temperatures (Fig. 13a).

15 Most of the proxy data cover the midlatitudes between 30 and 55° N/S (green bars in Fig. 13a). For low latitude proxies MIOC360 matches better than MIOC480 or  
20 MIOC720. Midlatitude proxies compare well with all experiments. The proxy data confirm that land temperatures were much warmer than today. Warmer high latitude temperatures as in MIOC720 are in better agreement with these proxy reconstructions. The midlatitudes are captured by all palaeo simulations, but cooler than present-day low latitude and warmer than present-day high latitudes cannot be captured together  
25 within one single experiment.

<a href="#">Title Page</a>	
<a href="#">Abstract</a>	<a href="#">Introduction</a>
<a href="#">Conclusions</a>	<a href="#">References</a>
<a href="#">Tables</a>	<a href="#">Figures</a>
<a href="#">◀</a>	<a href="#">▶</a>
<a href="#">◀</a>	<a href="#">▶</a>
<a href="#">Back</a>	<a href="#">Close</a>
<a href="#">Full Screen / Esc</a>	
<a href="#">Printer-friendly Version</a>	
<a href="#">Interactive Discussion</a>	



### 3.3.2 Marine Proxies

The isotopic composition of seawater, obtained by either  $\delta^{18}\text{O}$  or Mg/Ca ratios, facilitates a proxy for ocean temperatures (Emiliani and Edwards, 1953; Hastings et al., 1998). Using the calcite shells of fossil planktonic foraminifera deposited in the ocean sediments, sea surface temperatures (SSTs) for past times can be obtained.

We take Middle Miocene SST reconstruction from several Ocean Drilling Project (ODP) and Deep Sea Drilling Project (DSDP) sites (Table 4). Midlatitude SSTs agree well in all three simulations (Fig. 13b). MIOC360 and MIOC480 match (at least one) proxy-SST for low and high latitudes. The warmer than present high latitude SSTs are better captured in MIOC720, but low latitude SSTs are largely overestimated.

## 4 Summary and Discussion

We perform the first fully coupled simulations for the warm Middle Miocene using the general circulation model MPI-ESM. The Middle Miocene topography induces a global warming of 0.7 K compared to today. The continental warming is larger, because topography surely affects the continents, but not the ocean surface. Uncertainties in the applied topography can, therefore, significantly alter surface temperatures. Especially mountain regions like Andes, Rocky Mountains, and Himalayas are subject to errors in elevation (see Herold et al., 2008, Tables 1 and 2 for details).

If we increase atmospheric CO<sub>2</sub> levels to 480 and 720 ppm as in MIOC480 and MIOC720, we obtain a global warming of 2.8 and 4.9 K. A stronger greenhouse effect and the associated water vapour feedback lead to a more humid climate with an enhanced hydrological cycle. The climate sensitivity of 4.0 K is much larger than in previous studies, 2.0 K in You et al. (2009) and 2.3 K in Tong et al. (2009). The larger value may be explained by a higher climate sensitivity of the MPI-ESM compared to the model used by You et al. and Tong et al.

CPD

7, 1935–1972, 2011

## The Middle Miocene climate

M. Krapp and  
J. H. Jungclaus

[Title Page](#)

[Abstract](#)

[Introduction](#)

[Conclusions](#)

[References](#)

[Tables](#)

[Figures](#)

◀

▶

◀

▶

[Back](#)

[Close](#)

[Full Screen / Esc](#)

[Printer-friendly Version](#)

[Interactive Discussion](#)



Although MIOC480 and MIOC720 succeed to explain the estimated warming of 3–6 K (Tripati et al., 2009), both experiments fail to explain the flatter equator-to-pole temperature gradient (Nikolaev, 2006; Bruch et al., 2007). A comparison to proxy data shows that the low-latitude temperatures are too high and that the high-latitude temperatures are too low. Although sparser, marine proxies are more widely spread than terrestrial proxies, which are hardly available in the Southern Hemisphere, for example in Africa or in Australia. To improve model-data validation more low and high-latitude terrestrial proxies are needed. Tropical SST proxies may underestimate the signal, as studies for the Miocene and for the Eocene showed (Stewart et al., 2004; Pearson et al., 2007). A revision of the low-latitude marine proxies, especially those from older reconstructions, would be appropriate.

Although open ocean gateways support large-scale mixing between the adjacent ocean basins, against expectations, the AMOC in our model is insensitive to these water mass composition changes. In MIOC360 and MIOC480, the AMOC is as strong as today. It extends to the high latitudes, because the absent Greenland-Scotland Ridge cannot act as a barrier. The flow through the Panama Seaway is directed from the Pacific into the Atlantic, confirming the results of an idealised study for the early Miocene (von der Heydt and Dijkstra, 2006). Instead of a reduced salinity contrast between Pacific and Atlantic Ocean, we find a stronger salinity contrast. The slightly fresher Pacific Ocean is, therefore, not able to support deepwater formation as shown by von der Heydt and Dijkstra (2006). Previous model studies for an open Panama Seaway, reflecting the Pliocene period, report a collapse of the AMOC (Maier-Reimer et al., 1990), or a very weak overturning circulation (Lunt et al., 2007). In a recent review paper, Molnar (2008) discussed evidence from reconstructions and from model studies and concluded that the closing of the Panama Seaway “seems no more than a bit player in global climate change”. Of course, the situation in our simulations is different, because of the open Tethys. The Indian water input through the open Tethys could stabilise the AMOC. Only in MIOC720 where CO<sub>2</sub> levels are very high, the AMOC severely slows down. The topographic settings may differ from present-day, but none of

## The Middle Miocene climate

M. Krapp and  
J. H. Jungclaus

[Title Page](#)

[Abstract](#)

[Introduction](#)

[Conclusions](#)

[References](#)

[Tables](#)

[Figures](#)

◀

▶

◀

▶

[Back](#)

[Close](#)

[Full Screen / Esc](#)

[Printer-friendly Version](#)

[Interactive Discussion](#)



the IPCC AR4 models showed a collapse of the AMOC for A1B scenario, where CO<sub>2</sub> is gradually increased to 700 ppm comparable to MIOC720 (Schmittner et al., 2005). The IPCC AR4 version of the MPI-ESM shows a slow down of the AMOC by no more than 30 % (Jungclaus et al., 2006).

- 5 Just like the ocean circulation, the atmospheric circulation reorganises. Oceanic and atmospheric heat transport change, but the total heat transport remains nearly unchanged, because oceanic and atmospheric heat transport compensate. A reduction of the equator-to-pole temperature gradient is, therefore, unlikely caused by a reorganised ocean circulation, as it has been claimed earlier (Pagani et al., 1999). Instead,  
10 we find that changes in the local energy balance, for example due to a smaller surface albedo, a lower topography, or higher CO<sub>2</sub>, explain the warmer high latitudes.

Larger high latitude temperatures and higher atmospheric CO<sub>2</sub> levels provide good conditions for plant growth. Because our model includes a dynamic vegetation module, we are able to simulate the interactions and feedbacks between the vegetation  
15 and the climate system. We find that boreal forests expand northward into the high latitudes, which is in line with vegetation reconstructions (Wolfe, 1985; Williams et al., 2008). In contrast to that, the desert cover of the Saharan region disagrees with reconstructions (Senut et al., 2009). One problem is that the vegetation model JSBACH does not include a dynamic soil model. Some properties of the soils are, therefore,  
20 prescribed with present-day values. A recent model study shows that a dynamic background albedo scheme for JSBACH improves rainfall over the Sahel/Sahara region, which, applied to the mid Holocene (6000 yr ago), leads to higher vegetation variability (Vamborg et al., 2011). In a sensitivity study for the Late Miocene, Micheels et al.  
25 (2009) showed that a modern Sahara leads to a cooling in the northern high latitudes. We, therefore, expect a further high latitude warming if North Africa is covered by vegetation. Since the dense vegetation in our simulations requests warmer temperatures and higher CO<sub>2</sub> levels, we propose that the warm Middle Miocene climate depends on higher than present-day CO<sub>2</sub> levels.

## The Middle Miocene climate

M. Krapp and  
J. H. Jungclaus

[Title Page](#)

[Abstract](#)

[Introduction](#)

[Conclusions](#)

[References](#)

[Tables](#)

[Figures](#)

◀

▶

◀

▶

[Back](#)

[Close](#)

[Full Screen / Esc](#)

[Printer-friendly Version](#)

[Interactive Discussion](#)



## 5 Conclusions

- The Middle Miocene topography provides open ocean gateways that connect the major ocean basins. The ocean circulation and its associated poleward heat transport, therefore, reorganises. The atmosphere, however, compensates for the changed ocean  
5 heat transport, leaving the total heat transport nearly unaltered. Topographic changes alone do neither explain the warmer Middle Miocene climate nor the flatter equator-to-pole temperature gradient. We, therefore, rule out that the poleward heat transport can reduce the equator-to-pole temperature gradient. Instead, we propose that a stronger greenhouse effect, as a result of stronger than present CO<sub>2</sub> forcing, capture  
10 the warm Middle Miocene climate. Assuming higher atmospheric CO<sub>2</sub> levels, we are also able to reproduce the densely wooded Middle Miocene. Both high latitude vegetation feedbacks and the ice-albedo feedback lead to a polar amplification that reduces the equator-to-pole temperature gradient. Higher than present atmospheric CO<sub>2</sub> levels are, therefore, essential to drive the warm Middle Miocene climate.  
15 Acknowledgements. This work has been accomplished within the Project *Understanding Cenozoic Climate Cooling* of the German Research Foundation (DFG). All model integrations were performed at the high performance computing platforms of the German Climate Computing Centre (DKRZ) in Hamburg. We would like to thank Helmut Haak for helping to set up the model, Torsten Utescher for providing the terrestrial proxy data, and Victor Brovkin for  
20 proofreading the manuscript.

The service charges for this open access publication have been covered by the Max Planck Society.

## References

- 25 Blackmon, M.: A climatological spectral study of the 500 mb geopotential height of the Northern Hemisphere, J. Atmos. Sci., 33, 1607–1623, doi:10.1175/1520-0469(1976)033<1607:ACSSOT>2.0.CO;2, 1976. 1941

## The Middle Miocene climate

M. Krapp and  
J. H. Jungclaus

Title Page

Abstract

Introduction

Conclusions

References

Tables

Figures

◀

▶

◀

▶

Back

Close

Full Screen / Esc

Printer-friendly Version

Interactive Discussion



## The Middle Miocene climate

M. Krapp and  
J. H. Jungclaus

[Title Page](#)

[Abstract](#)

[Introduction](#)

[Conclusions](#)

[References](#)

[Tables](#)

[Figures](#)

◀

▶

◀

▶

[Back](#)

[Close](#)

[Full Screen / Esc](#)

[Printer-friendly Version](#)

[Interactive Discussion](#)



Böhme, M., Winklhofer, M., and Ilg, A.: Miocene precipitation in Europe: temporal trends and spatial gradients, *Palaeogeogr. Palaeoclimatol. Palaeoecol.*, 304, 212–218, doi:10.1016/j.palaeo.2010.09.028, 2011. 1936

5 Brovkin, V., Raddatz, T., Reick, C., Claussen, M., and Gayler, V.: Global biogeophysical interactions between forest and climate, *Geophys. Res. Lett.*, 36, L07405, doi:10.1029/2009GL037543, 2009. 1938

Bruch, A., Uhl, D., and Mosbrugger, V.: Miocene climate in Europe—Patterns and evolution: a first synthesis of NECLIME, *Palaeogeogr. Palaeoclimatol. Palaeoecol.*, 253, 1–7, doi:10.1016/j.palaeo.2007.03.030, 2007. 1936, 1948

10 Bruch, A., Utzinger, T., and Mosbrugger, V.: Precipitation patterns in the Miocene of Central Europe and the development of continentality, *Palaeogeogr. Palaeoclimatol. Palaeoecol.*, 304, 202–211, doi:10.1016/j.palaeo.2010.10.002, 2010. 1936, 1941

Douglas, R. and Savin, S.: Isotopic analysis of planktonic foraminifera from the cenozoic of the Northwest Pacific, leg 6, *Initial Rep. Deep Sea*, 6, 1123–1127, doi:10.2973/dsdp.proc.6.1971, 1971. 1959

15 Emiliani, C. and Edwards, G.: Tertiary ocean bottom temperatures, *Nature*, 171, 887–888, 1953. 1947

Ennyu, A.: Middle Miocene climate evolution in the pacific realm, Ph.D. thesis, The Pennsylvania State University, University Park, PA, 2003. 1959

20 Ennyu, A. and Arthur, M.: The Cenozoic Southern Ocean: tectonics, sedimentation, and climate change between Australia and Antarctica, chap. Early to Middle Miocene Paleoceanography in the Southern High Latitudes Off Tasmania, p. 215, American Geophysical Union, Washington, DC, 2004. 1959

Hastings, D., Russell, A., and Emerson, S.: Foraminiferal magnesium in Globigerinoides sacculifer as a paleotemperature proxy, *Paleoceanography*, 13, 161–169, doi:10.1029/97PA03147, 1998. 1947

25 Heinemann, M., Jungclaus, J. H., and Marotzke, J.: Warm Paleocene/Eocene climate as simulated in ECHAM5/MPI-OM, *Clim. Past*, 5, 785–802, doi:10.5194/cp-5-785-2009, 2009. 1944

Henrot, A.-J., François, L., Favre, E., Butzin, M., Ouberrous, M., and Munhoven, G.: Effects 30 of CO<sub>2</sub>, continental distribution, topography and vegetation changes on the climate at the Middle Miocene: a model study, *Clim. Past*, 6, 675–694, doi:10.5194/cp-6-675-2010, 2010. 1937, 1940, 1943, 1958

Herold, N., Seton, M., Müller, R., You, Y., and Huber, M.: Middle Miocene tectonic

## The Middle Miocene climate

M. Krapp and  
J. H. Jungclaus

[Title Page](#)

[Abstract](#)

[Introduction](#)

[Conclusions](#)

[References](#)

[Tables](#)

[Figures](#)

◀

▶

◀

▶

[Back](#)

[Close](#)

[Full Screen / Esc](#)

[Printer-friendly Version](#)

[Interactive Discussion](#)



- boundary conditions for use in climate models, *Geochem. Geophys. Geosy.*, 9, Q10009, doi:10.1029/2008GC002046, 2008. 1938, 1947
- Herold, N., Müller, R., and Seton, M.: Comparing early to middle Miocene terrestrial climate simulations with geological data, *Geosphere*, 6, 952–961, doi:10.1130/GES00544.1, 2010. 1937
- von der Heydt, A. and Dijkstra, H.: Effect of ocean gateways on the global ocean circulation in the late Oligocene and early Miocene, *Paleoceanography*, 21, PA1011, doi:10.1029/2005PA001149, 2006. 1948
- Hibler, W.: A dynamic thermodynamic sea ice model, *J. Phys. Oceanogr.*, 9, 815–846, doi:10.1175/1520-0485(1979)009<0815:ADTSIM>2.0.CO;2, 1979. 1938
- Jungclaus, J., Botzet, M., Haak, H., Marotzke, J., Mikolajewicz, U., Roeckner, E., Keenlyside, N., Latif, M., and Luo, J.: Ocean circulation and tropical variability in the coupled model ECHAM5/MPI-OM, *J. Climate*, 19, 3952–3972, doi:10.1175/JCLI3827.1, 2006. 1949
- Krylov, A., Andreeva, I., Vogt, C., Backman, J., Krupskaya, V., Grikurov, G., Moran, K., and Shoji, H.: A shift in heavy and clay mineral provenance indicates a Middle Miocene onset of a perennial sea ice cover in the Arctic Ocean, *Paleoceanography*, 23, PA1S06, doi:10.1029/2007PA001497, 2008. 1943
- Kuhnert, H., Bickert, T., and Paulsen, H.: Southern Ocean frontal system changes precede Antarctic ice sheet growth during the Middle Miocene, *Earth Planet. Sc. Lett.*, 284, 630–638, doi:10.1016/j.epsl.2009.05.030, 2009. 1959
- Kürschner, W., Kvaček, Z., and Dilcher, D.: The impact of Miocene atmospheric carbon dioxide fluctuations on climate and the evolution of terrestrial ecosystems, *P. Natl. Acad. Sci. USA*, 105, 449, doi:10.1073/pnas.0708588105, 2008. 1937
- Lunt, D., Valdes, P., Haywood, A., and Rutt, I.: Closure of the Panama Seaway during the Pliocene: implications for climate and Northern Hemisphere glaciation, *Clim. Dynam.*, 30, 1–18, doi:10.1007/s00382-007-0265-6, 2007. 1942, 1948
- Maier-Reimer, E., Mikolajewicz, U., and Crowley, T.: Ocean general circulation model sensitivity experiment with an open Central American Isthmus, *Paleoceanography*, 5, 349–366, doi:10.1029/PA005i003p00349, 1990. 1942, 1948
- Majewski, W.: Planktonic foraminiferal response to Middle Miocene cooling in the Southern Ocean (ODP site 747, Kerguelen Plateau), *Acta Palaeontol. Pol.*, 55, 541–560, doi:10.4202/app.2009.0088, 2010. 1959
- Marsland, S. J., Haak, H., Jungclaus, J. H., Latif, M., and Röske, F.: The Max-Planck-Institute

## The Middle Miocene climate

M. Krapp and  
J. H. Jungclaus

[Title Page](#)

[Abstract](#)

[Introduction](#)

[Conclusions](#)

[References](#)

[Tables](#)

[Figures](#)

◀

▶

◀

▶

[Back](#)

[Close](#)

[Full Screen / Esc](#)

[Printer-friendly Version](#)

[Interactive Discussion](#)



- global ocean/sea ice model with orthogonal curvilinear coordinates, *Ocean Model.*, 5, 91–127, doi:10.1016/S1463-5003(02)00015-X, 2003. 1938
- Micheels, A., Eronen, J., and Mosbrugger, V.: The Late Miocene climate response to a modern Sahara desert, *Global Planet. Change*, 67, 193–204, doi:10.1016/j.gloplacha.2009.02.005, 2009. 1949
- 5 Molnar, P.: Closing of the Central American Seaway and the Ice Age: a critical review, *Paleoceanography*, 23, PA2201, doi:10.1029/2007PA001574, 2008. 1948
- Mosbrugger, V. and Utescher, T.: The coexistence approach – a method for quantitative reconstructions of Tertiary terrestrial palaeoclimate data using plant fossils, *Palaeogeogr. Palaeoclimatol. Palaeoecol.*, 134, 61–86, 1997. 1946
- 10 Myhre, G., Highwood, E., Shine, K., and Stordal, F.: New estimates of radiative forcing due to well mixed greenhouse gases, *Geophys. Res. Lett.*, 25, 2715–2718, doi:10.1029/98GL01908, 1998. 1937
- Nikolaev, S.: Principal features of the World Ocean climate change in the Cenozoic and their 15 possible causes, *Oceanology*, 46, 513–525, doi:10.1134/S0001437006040084, 2006. 1936, 1948
- Oleinik, A., Marincovich, Jr., L. K., and Swart, P.: Magnitude of Middle Miocene warming in North Pacific high latitudes: stable isotope evidence from Kaneharaia (Bivalvia, Dosiniinae), *Bull. Geol. Surv. Jap.*, 59, 339–353, 2008. 1959
- 20 Pagani, M., Arthur, M., and Freeman, K.: Miocene evolution of atmospheric carbon dioxide, *Paleoceanography*, 14, 273–292, doi:10.1029/1999PA900006, 1999. 1937, 1949, 1959
- Pearson, P., Van Dongen, B., Nicholas, C., Pancost, R., Schouten, S., Singano, J., and Wade, B.: Stable warm tropical climate through the Eocene Epoch, *Geology*, 35, 211–214, doi:10.1130/G23175A.1, 2007. 1948
- 25 Raddatz, T., Reick, C., Knorr, W., Kattge, J., Roeckner, E., Schnur, R., Schnitzler, K., Wetzel, P., and Jungclaus, J.: Will the tropical land biosphere dominate the climate–carbon cycle feedback during the twenty-first century?, *Clim. Dynam.*, 29, 565–574, doi:10.1007/s00382-007-0247-8, 2007. 1938
- Raymo, M.: The Himalayas, organic carbon burial, and climate in the Miocene, *Paleoceanography*, 9, 399–404, doi:10.1029/94PA00289, 1994. 1939
- 30 Roeckner, E., Bäuml, G., Bonaventura, L., Brokopf, R., and Esch, M.: The Atmospheric General Circulation Model Echam5. Part I: Model Description, Tech. rep., Max-Planck Institute for Meteorology, Hamburg, 2003. 1938

Roeckner, E., Brokopf, R., Esch, M., Giorgetta, M., Hagemann, S., Kornblueh, L., Manzini, E., Schlese, U., and Schulzweida, U.: Sensitivity of simulated climate to horizontal and vertical resolution in the ECHAM5 atmosphere model, *J. Climate*, 19, 3771–3791, 2006. 1956

Royer, D., Wing, S., Beerling, D., Jolley, D., Koch, P., Hickey, L., and Berner, R.: Paleobotanical evidence for near present-day levels of atmospheric CO<sub>2</sub> during part of the Tertiary, *Science*, 292, 2310–2313, doi:10.1126/science.292.5525.2310, 2001. 1937

Savin, S., Douglas, R., and Stehlí, F.: Tertiary marine paleotemperatures, *Bull. Geol. Soc. Am.*, 86, 1499–1510, doi:10.1130/0016-7606(1975)86<1499:TMP>2.0.CO;2, 1975. 1959

Schmittner, A., Latif, M., and Schneider, B.: Model projections of the North Atlantic thermo-haline circulation for the 21st century assessed by observations, *Geophys. Res. Lett.*, 32, L23710, doi:10.1029/2005GL024368, 2005. 1949

Semetner, A. J.: A model for the thermodynamic growth of sea ice in numerical investigations of climate, *J. Phys. Oceanogr.*, 6, 379–389, doi:10.1175/1520-0485(1976)006<0379:AMFTTG>2.0.CO;2, 1976. 1938

Senut, B., Pickford, M., and Ségalen, L.: Neogene desertification of Africa, *C. R. Geosci.*, 341, 591–602, doi:10.1016/j.crte.2009.03.008, 2009. 1936, 1945, 1949

Shackleton, N. and Kennett, J.: Paleotemperature history of the Cenozoic and the initiation of Antarctic Glaciation: oxygen and carbon isotope analyses in DSDP sites 277, 279 and 281, *Initial Rep. Deep Sea*, 29, 743–755, doi:10.2973/dsdp.proc.29.1975, 1975. 1959

Shevenell, A., Kennett, J., and Lea, D.: Middle Miocene Southern Ocean cooling and Antarctic cryosphere expansion, *Science*, 305, 1766–1770, doi:10.1126/science.1100061, 2004. 1959

van der Smissen, J. and Rullkötter, J.: Organofacies variations in sediments from the continental slope and rise of the New Jersey continental margin (Sites 903 and 905), in: *Proceedings of the Ocean Drilling Program. Scientific results*, doi:10.2973/odp.proc.sr.150.040.1996, 1996. 1959

Stewart, D., Pearson, P., Ditchfield, P., and Singano, J.: Miocene tropical Indian Ocean temperatures: evidence from three exceptionally preserved foraminiferal assemblages from Tanzania, *J. Afr. Earth Sci.*, 40, 173–189, doi:10.1016/j.jafrearsci.2004.09.001, 2004. 1948

Tong, J., You, Y., Müller, R., and Seton, M.: Climate model sensitivity to atmospheric CO<sub>2</sub> concentrations for the Middle Miocene, *Global Planet. Change*, 67, 129–140, doi:10.1016/j.gloplacha.2009.02.001, 2009. 1937, 1939, 1940, 1943, 1947, 1958

Tripati, A., Roberts, C., and Eagle, R.: Coupling of CO<sub>2</sub> and ice sheet stability

## The Middle Miocene climate

M. Krapp and  
J. H. Jungclaus

[Title Page](#)

[Abstract](#) [Introduction](#)

[Conclusions](#) [References](#)

[Tables](#) [Figures](#)



[Back](#) [Close](#)

[Full Screen / Esc](#)

[Printer-friendly Version](#)

[Interactive Discussion](#)



## The Middle Miocene climate

M. Krapp and  
J. H. Jungclaus

[Title Page](#)

[Abstract](#)

[Introduction](#)

[Conclusions](#)

[References](#)

[Tables](#)

[Figures](#)

◀

▶

◀

▶

[Back](#)

[Close](#)

[Full Screen / Esc](#)

[Printer-friendly Version](#)

[Interactive Discussion](#)



- over major climate transitions of the last 20 million years, *Science*, 326, 1394–1397, doi:10.1126/science.1178296, 2009. 1936, 1948
- Uppala, S. M., Källberg, P. W., Simmons, A. J., Andrae, U., Bechtold, V. D. C., Fiorino, M., Gibson, J. K., Haseler, J., Hernandez, A., Kelly, G. A., Li, X., Onogi, K., Saarinen, S., Sokka, N., Allan, R. P., Andersson, E., Arpe, K., Balmaseda, M. A., Beljaars, A. C. M., Berg, L. V. D., Bidlot, J., Bormann, N., Caires, S., Chevallier, F., Dethof, A., Dragosavac, M., Fisher, M., Fuentes, M., Hagemann, S., Hölm, E., Hoskins, B. J., Isaksen, L., Janssen, P. A. E. M., Jenne, R., McNally, A. P., Mahfouf, J.-F., Morcrette, J.-J., Rayner, N. A., Saunders, R. W., Simon, P., Sterl, A., Trenberth, K. E., Untch, A., Vasiljevic, D., Viterbo, P., and Woollen, J.: The ERA-40 re-analysis, *Q. J. Roy. Meteor. Soc.*, 131, 2961–3012, doi:10.1256/qj.04.176, 2005. 1939
- Utescher, T., Böhme, M., and Mosbrugger, V.: The Neogene of Eurasia: spatial gradients and temporal trends—the second synthesis of NECLIME, *Palaeogeogr. Palaeoclimatol. Palaeoecol.*, 304, 196–201, doi:10.1016/j.palaeo.2011.03.012, 2011. 1946
- Valcke, S.: OASIS3 User Guide (prism\_2-5), Tech. Rep. 3, PRISM, available at: [http://www.prism.enes.org/PAEs/coupling\\_IO/software\\_OASIS3.php](http://www.prism.enes.org/PAEs/coupling_IO/software_OASIS3.php) (last access: June 2011), 2006. 1938
- Vamborg, F. S. E., Brovkin, V., and Claussen, M.: The effect of a dynamic background albedo scheme on Sahel/Sahara precipitation during the mid-Holocene, *Clim. Past*, 7, 117–131, doi:10.5194/cp-7-117-2011, 2011. 1949
- Williams, C. J., Mendell, E. K., Murphy, J., Court, W. M., Johnson, A. H., and Richter, S. L.: Paleoenvironmental reconstruction of a Middle Miocene forest from the Western Canadian Arctic, *Palaeogeogr. Palaeoclimatol. Palaeoecol.*, 261, 160–176, doi:10.1016/j.palaeo.2008.01.014, 2008. 1936, 1949
- Wolfe, J.: The Carbon Cycle and Atmospheric CO<sub>2</sub>: Natural Variations Archean to Present, chap. Distribution of major vegetational types during the Tertiary, American Geophysical Union, Washington, DC, pp. 357–375, 1985. 1936, 1945, 1949
- You, Y., Huber, M., Müller, D., Poulsen, C., and Ribbe, J.: Simulation of the Middle Miocene climate optimum, *Geophys. Res. Lett.*, 36, L04702, doi:10.1029/2008GL036571, 2009. 1937, 1939, 1940, 1943, 1947, 1958
- Zachos, J., Pagani, M., Sloan, L., Thomas, E., and Billups, K.: Trends, rhythms, and aberrations in global climate 65 Ma to present, *Science*, 292, 686–693, doi:10.1126/science.1059412, 2001. 1936, 1937

## The Middle Miocene climate

M. Krapp and  
J. H. Jungclaus

**Table 1.** RMSEs with respect to ERA-40 (1979–1993) for temperature  $T$  (in  $^{\circ}\text{C}$ ), geopotential height  $Z$  (in dam), and zonal wind  $U$  (in  $\text{m s}^{-1}$ ) at pressure levels 200, 500, and 850 hPa, and sea level pressure SLP (in hPa). RMSEs in Roeckner et al. (2006) are for ECHAM5 in T42L19 (same resolution as used here) with respect to ERA-15. The RMSE differences between ERA-15 and ERA-40 are taken from Table 2, Roeckner et al. (2006).

variable	T200	T500	T850	Z200	Z500	Z850	SLP	U200	U500	U850
CTRL	6.47	1.13	2.46	7.98	4.41	2.08	3.99	4.71	2.61	2.10
Roeckner et al. (2006)	5.12	1.00	2.02	7.04	3.25	1.93	2.55	4.48	2.37	1.92
ERA-15	0.68	0.40	1.08	0.83	0.67	0.56	1.25	0.73	0.85	0.61

**The Middle Miocene climate**M. Krapp and  
J. H. Jungclaus[Title Page](#)[Abstract](#)[Introduction](#)[Conclusions](#)[References](#)[Tables](#)[Figures](#)[◀](#)[▶](#)[◀](#)[▶](#)[Back](#)[Close](#)[Full Screen / Esc](#)[Printer-friendly Version](#)[Interactive Discussion](#)**Table 2.** Global mean climate parameters for all experiments. Sea ice parameters are calculated for the Northern Hemisphere.

climate parameter	CTRL	MIOC360	MIOC480	MIOC720
2 m air temperature in °C	14.3	15.0	17.1	19.2
1000 hPa temperature in °C	14.6	15.1	17.1	19.2
global surface temperature in °C	15.1	15.8	17.7	19.8
land surface temperature in °C	9.3	10.5	12.9	15.7
sea surface temperature in °C	18.0	18.3	19.8	21.4
total precipitation in mm a <sup>-1</sup>	1082	1080	1103	1131
total cloud cover	0.617	0.616	0.604	0.591
sea level pressure in hPa	1011	1004	1004	1004
vertically integrated water vapour in kg m <sup>-2</sup>	26.3	26.8	30.5	35.8
long-wave emissivity $\varepsilon$	0.582	0.580	0.569	0.557
planetary albedo $\alpha$	0.320	0.317	0.312	0.306
sea ice area (Mar) in 10 <sup>6</sup> km <sup>2</sup>	14.9	14.3	11.7	9.9
sea ice area (Sep) in 10 <sup>6</sup> km <sup>2</sup>	6.7	4.6	1.2	0.17
sea ice volume (Mar) in 10 <sup>3</sup> km <sup>3</sup>	35.9	21.7	13.3	8.4
sea ice volume (Sep) in 10 <sup>3</sup> km <sup>3</sup>	16.1	4.6	0.4	0.07
global forest cover in 10 <sup>6</sup> km <sup>2</sup>	57.9	59.5	63.4	63.7
global desert cover in 10 <sup>6</sup> km <sup>2</sup> (55° S – 55° N)	17.0	15.3	14.5	16.4

## The Middle Miocene climate

M. Krapp and  
J. H. Jungclaus

**Table 3.** Global mean temperature  $T$  (in  $^{\circ}\text{C}$ ) and precipitation  $P$  (in  $\text{mm a}^{-1}$ ) of our Middle Miocene experiments compared to corresponding experiments of previous model studies. Boldface indicate values that are within one standard deviation of the global annual mean.

	$T_{2\text{m}}$	$T_{\text{surf}}$	$T_{\text{land}}$	$T_{\text{ocean}}$	$P$
MIOC360		15.8	10.5		
SM_350 (You et al., 2009)		17.0			
SH_350 (You et al., 2009)		17.8	16.2		
MIOC480	17.1	17.7		19.8	1103
MidCO <sub>2</sub> (Tong et al., 2009)		15.9			1080
MM4-veg (Henrot et al., 2010)	15.7			17.7	<b>1114</b>
MIOC720		19.8		21.4	1131
HighCO <sub>2</sub> (Tong et al., 2009)		18.2			1097
SM_700 (You et al., 2009)		19.0		20.5	
SH_700 (You et al., 2009)		<b>19.8</b>			

[Title Page](#)[Abstract](#)[Introduction](#)[Conclusions](#)[References](#)[Tables](#)[Figures](#)[◀](#)[▶](#)[◀](#)[▶](#)[Back](#)[Close](#)[Full Screen / Esc](#)[Printer-friendly Version](#)[Interactive Discussion](#)

## The Middle Miocene climate

M. Krapp and  
J. H. Jungclaus

**Table 4.** References of marine proxy SST reconstructions.

source	reference
DSDP 55	Douglas and Savin (1971)
DSDP 167	Savin et al. (1975)
DSDP 279A and 281	Shackleton and Kennett (1975)
ODP 903 and 905	van der Smissen and Rulkötter (1996)
DSDP 588, 608, and ODP 730	Pagani et al. (1999)
DSDP 588, 608, and ODP 883	Ennyu (2003)
ODP 1170 and 1172	Ennyu and Arthur (2004)
ODP 1170 and 1171	Shevenell et al. (2004)
ODP 1092	Kuhnert et al. (2009)
ODP 747	Majewski (2010)
bivalvia shells	Oleinik et al. (2008)
bivalvia shells	Ennyu (2003)

- [Title Page](#)
- [Abstract](#) | [Introduction](#)
- [Conclusions](#) | [References](#)
- [Tables](#) | [Figures](#)
- [◀](#) | [▶](#)
- [◀](#) | [▶](#)
- [Back](#) | [Close](#)
- [Full Screen / Esc](#)
- [Printer-friendly Version](#)
- [Interactive Discussion](#)

## The Middle Miocene climate

M. Krapp and  
J. H. Jungclaus

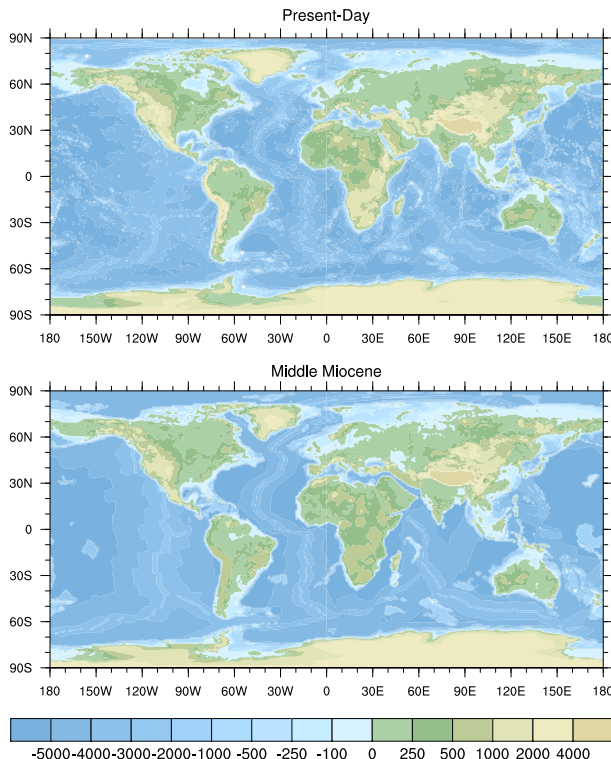


**Fig. 1.** The present-day topography we use in CTRL, and the Middle Miocene topography we use in MIOC360, MIOC480, and MIOC720.

[Title Page](#)

[Abstract](#)

[Introduction](#)

[Conclusions](#)

[References](#)

[Tables](#)

[Figures](#)

[◀](#)

[▶](#)

[◀](#)

[▶](#)

[Back](#)

[Close](#)

[Full Screen / Esc](#)

[Printer-friendly Version](#)

[Interactive Discussion](#)



## The Middle Miocene climate

M. Krapp and  
J. H. Jungclaus

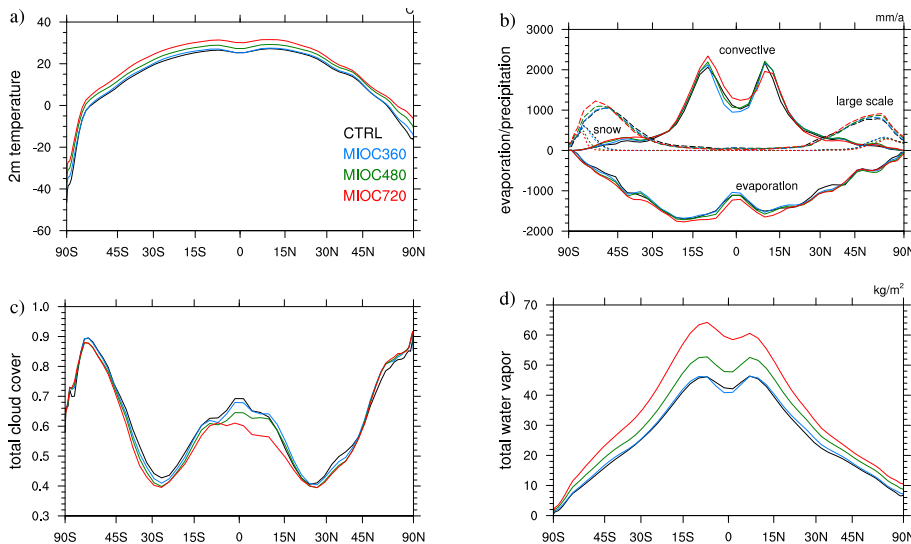


**Fig. 2.** **(a)** Zonally averaged 2 m air temperature (in °C). **(b)** Zonally averaged convective precipitation, large-scale precipitation, snow fall, and evaporation (in mm a<sup>-1</sup>). **(c)** Zonally averaged cloud cover. **(d)** Zonally averaged total water vapour content of the atmosphere (in kg m<sup>-2</sup>).

[Title Page](#)

[Abstract](#)

[Introduction](#)

[Conclusions](#)

[References](#)

[Tables](#)

[Figures](#)

[◀](#)

[▶](#)

[◀](#)

[▶](#)

[Back](#)

[Close](#)

[Full Screen / Esc](#)

[Printer-friendly Version](#)

[Interactive Discussion](#)

## The Middle Miocene climate

M. Krapp and  
J. H. Jungclaus

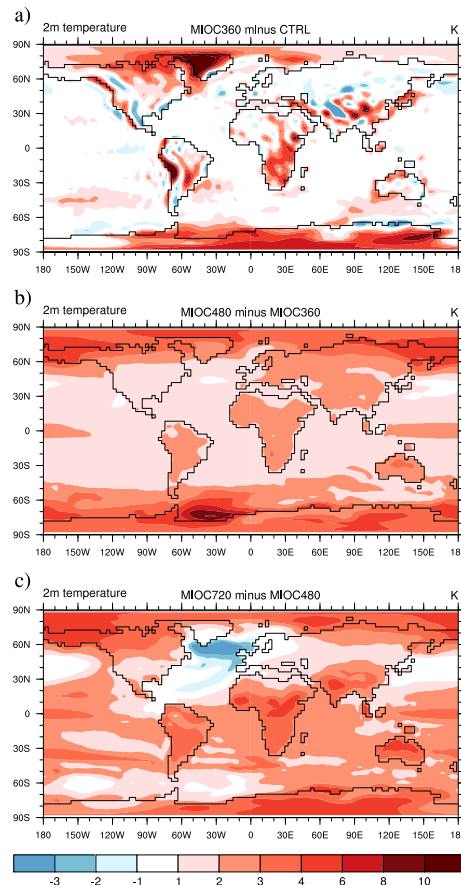


**Fig. 3.** Differences in 2 m air temperature between (a) MIOC360 and CTRL, (b) MIOC480 and MIOC360, and (c) between MIOC720 and MIOC480 (in K).

## The Middle Miocene climate

M. Krapp and  
J. H. Jungclaus

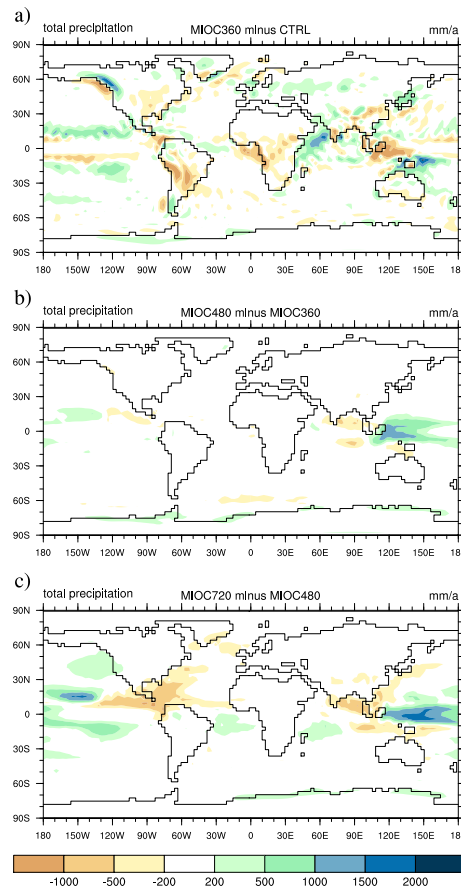


**Fig. 4.** Differences in total precipitation between (a) MIOC360 and CTRL, (b) MIOC480 and MIOC360, and (c) between MIOC720 and MIOC480 (in  $\text{mm a}^{-1}$ ).

[Title Page](#)

[Abstract](#)

[Introduction](#)

[Conclusions](#)

[References](#)

[Tables](#)

[Figures](#)

◀

▶

◀

▶

[Back](#)

[Close](#)

[Full Screen / Esc](#)

[Printer-friendly Version](#)

[Interactive Discussion](#)



## The Middle Miocene climate

M. Krapp and  
J. H. Jungclaus

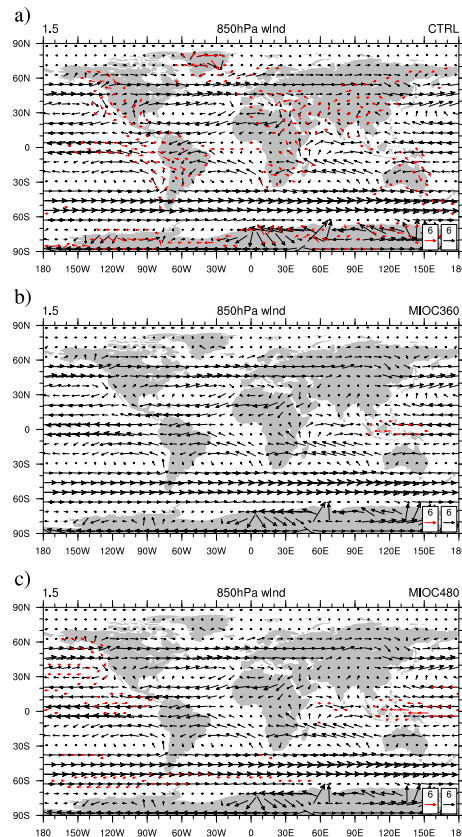


**Fig. 5.** Low level wind field in (a) CTRL (black arrows) and the difference to MIOC360 (red arrows), (b) MIOC360 and the difference to MIOC480, and (c) MIOC480 and the difference to MIOC480. The lower right reference arrows correspond to a velocity of  $6 \text{ m s}^{-1}$ .

## The Middle Miocene climate

M. Krapp and  
J. H. Jungclaus

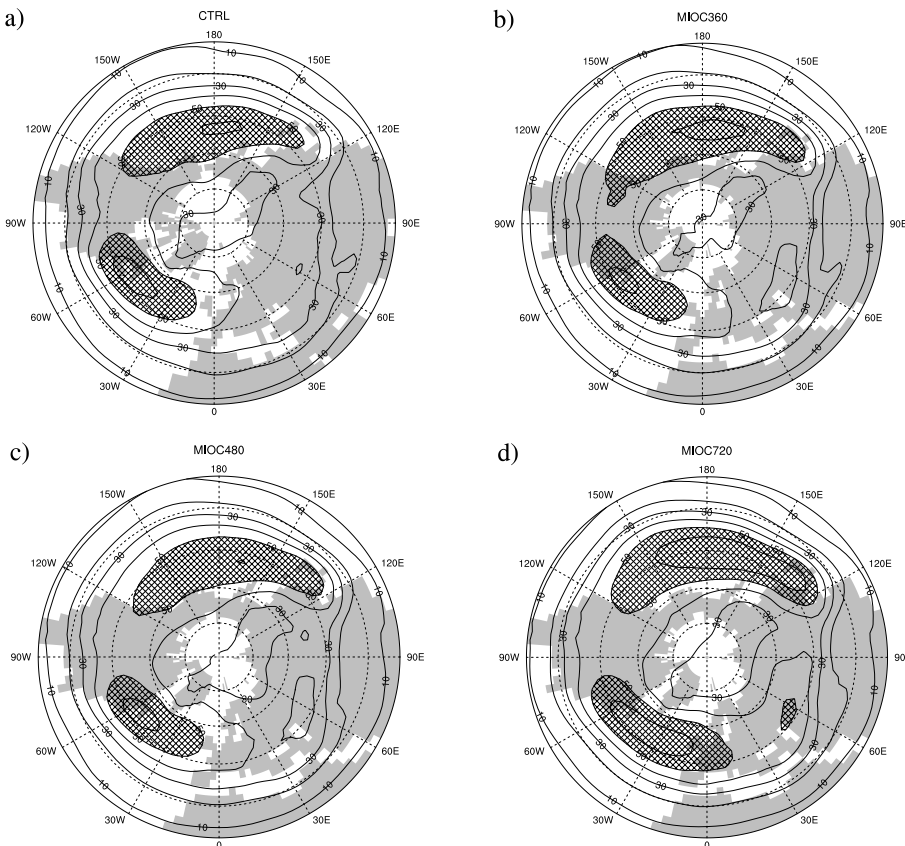


**Fig. 6.** Winter storm tracks defined as deviations of the 2–6 days bandpass-filtered 500 hPa geopotential height from December to March for (a) CTRL, (b) MIOC360, (c) MIOC480, and (d) MIOC720 (in gpm). Contour interval is every 10 gpm. Stippled regions indicate mean deviations that are larger than 50 gpm.

[Title Page](#)

[Abstract](#)

[Introduction](#)

[Conclusions](#)

[References](#)

[Tables](#)

[Figures](#)



[Back](#)

[Close](#)

[Full Screen / Esc](#)

[Printer-friendly Version](#)

[Interactive Discussion](#)

## The Middle Miocene climate

M. Krapp and  
J. H. Jungclaus

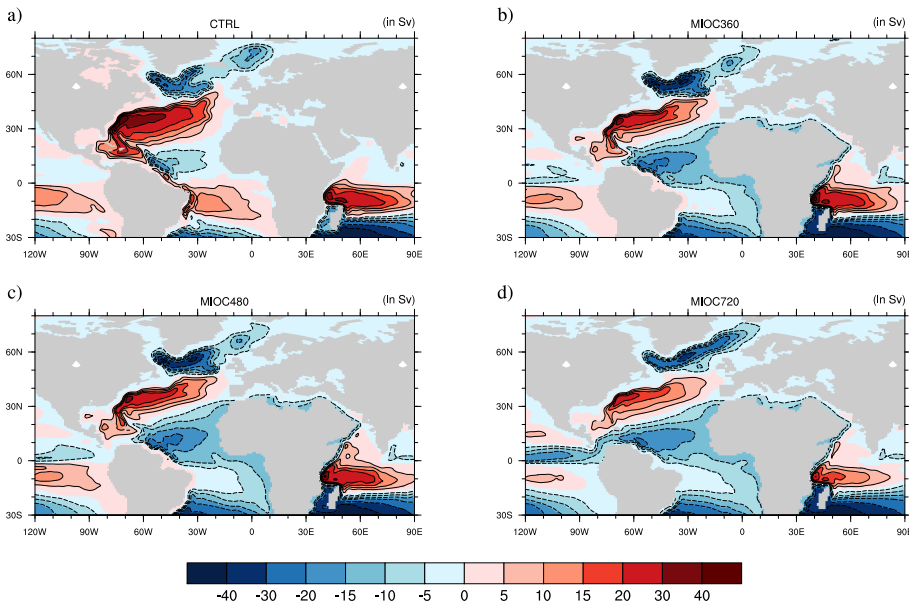


**Fig. 7.** Horizontal ocean circulation in the Atlantic Ocean in terms of the barotropic streamfunction for (a) CTRL, (b) MIOC360, (c) MIOC480, and (d) MIOC720 (in Sv).

[Title Page](#)

[Abstract](#)

[Introduction](#)

[Conclusions](#)

[References](#)

[Tables](#)

[Figures](#)



[Back](#)

[Close](#)

[Full Screen / Esc](#)

[Printer-friendly Version](#)

[Interactive Discussion](#)



## The Middle Miocene climate

M. Krapp and  
J. H. Jungclaus

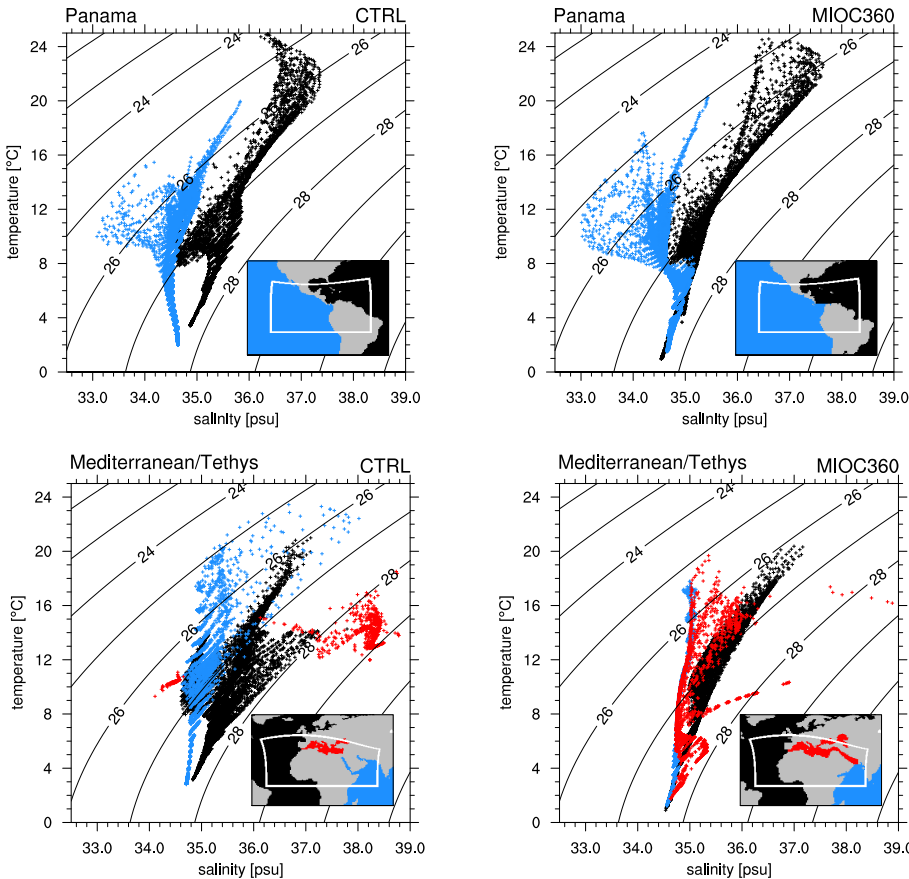


**Fig. 8.** T-S diagram for the water masses below 150 m in the vicinity of the Panama Seaway (top) and the Mediterranean/Tethys (bottom) for CTRL (left) and MIOC360 (right). Black crosses represent Atlantic Ocean water masses, blue crosses Pacific and Indian Ocean water, and red crosses Mediterranean/Tethys water. The in-line plots show the region for which the T-S pairs are obtained.

[Title Page](#)

[Abstract](#)

[Introduction](#)

[Conclusions](#)

[References](#)

[Tables](#)

[Figures](#)

◀

▶

◀

▶

[Back](#)

[Close](#)

[Full Screen / Esc](#)

[Printer-friendly Version](#)

[Interactive Discussion](#)

## The Middle Miocene climate

M. Krapp and  
J. H. Jungclaus

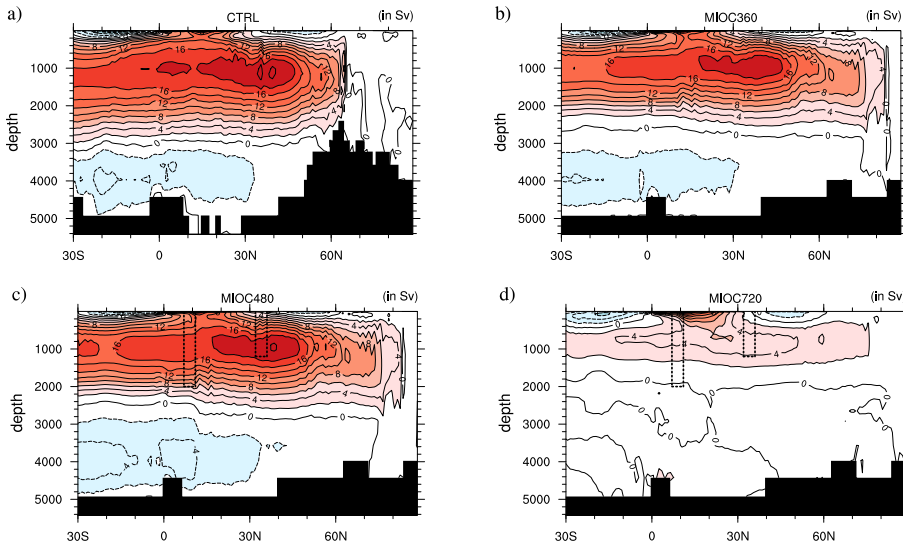


**Fig. 9.** Meridional overturning circulation in the Atlantic Ocean for **(a)** CTRL, **(b)** MIOC360, **(c)** MIOC480, and **(d)** MIOC720 (in Sv). Contour interval is 2 Sv. Red corresponds to clockwise circulation; blue corresponds to anti-clockwise circulation. The rectangular boxes indicate the Middle Miocene ocean gateways: Panama Seaway at 10° N and Tethys Throughflow at 35° N. Note the subsided Greenland-Scotland Ridge for the Middle Miocene experiments.

[Title Page](#)

[Abstract](#)

[Introduction](#)

[Conclusions](#)

[References](#)

[Tables](#)

[Figures](#)

◀

▶

◀

▶

[Back](#)

[Close](#)

[Full Screen / Esc](#)

[Printer-friendly Version](#)

[Interactive Discussion](#)

## The Middle Miocene climate

M. Krapp and  
J. H. Jungclaus

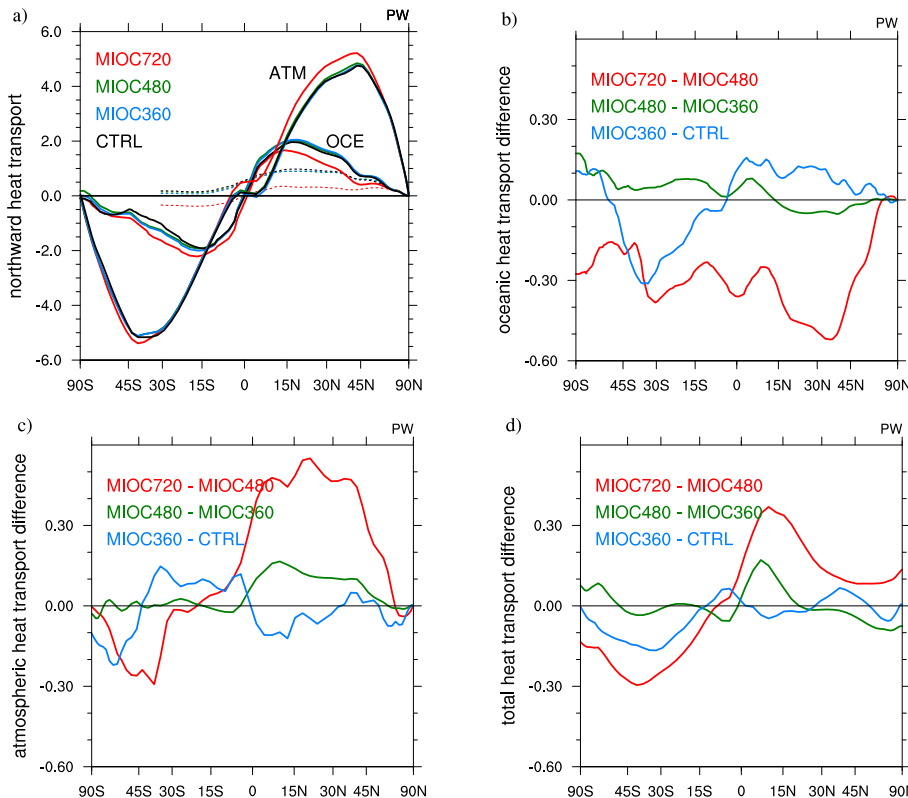


**Fig. 10.** (a) Northward heat transport by atmosphere and ocean (in PW). Dashed lines correspond to heat transport by the Atlantic Ocean. Difference in the (b) oceanic heat transport, (c) the atmospheric heat transport, and (d) the total (atmosphere + ocean) heat transport. Note the different scale in the difference plots (b–d).

## The Middle Miocene climate

M. Krapp and  
J. H. Jungclaus

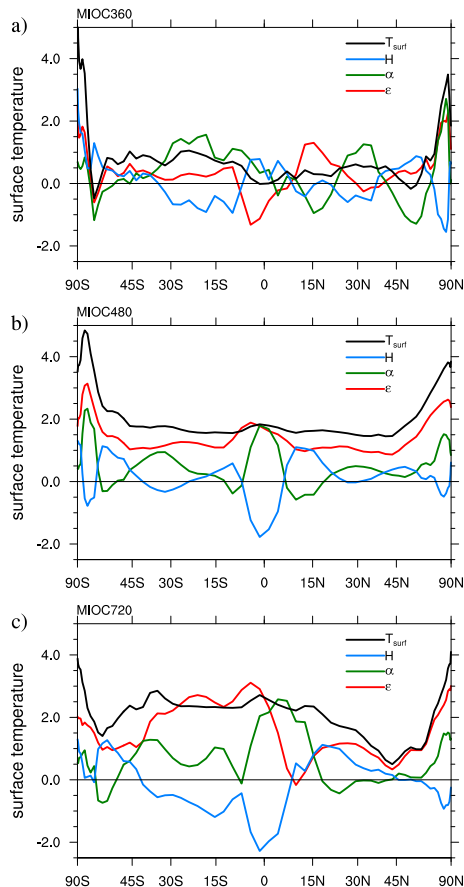


**Fig. 11.** Contribution of  $\alpha$ ,  $\epsilon$ , and  $H$  to changes in the zonally averaged surface temperature  $T_{\text{surf}}$  according to Eq. (1). Temperature increase in **(a)** MIOC360 compared to CTRL, **(b)** MIOC480 compared to MIOC360, and **(c)** MIOC720 compared to MIOC480.

## The Middle Miocene climate

M. Krapp and  
J. H. Jungclaus

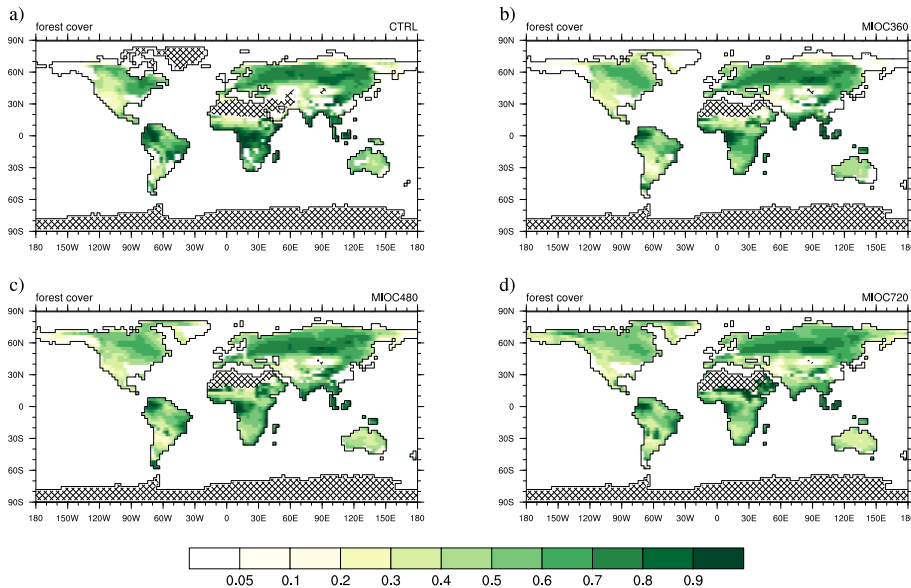


**Fig. 12.** Forest cover fraction for (a) CTRL, (b) MIOC360, (c) MIOC480, and (d) MIOC720. Crosshatched areas represent desert regions, including land ice, that cover more than 75 %.

[Title Page](#)

[Abstract](#)

[Introduction](#)

[Conclusions](#)

[References](#)

[Tables](#)

[Figures](#)



[Back](#)

[Close](#)

[Full Screen / Esc](#)

[Printer-friendly Version](#)

[Interactive Discussion](#)

## The Middle Miocene climate

M. Krapp and  
J. H. Jungclaus

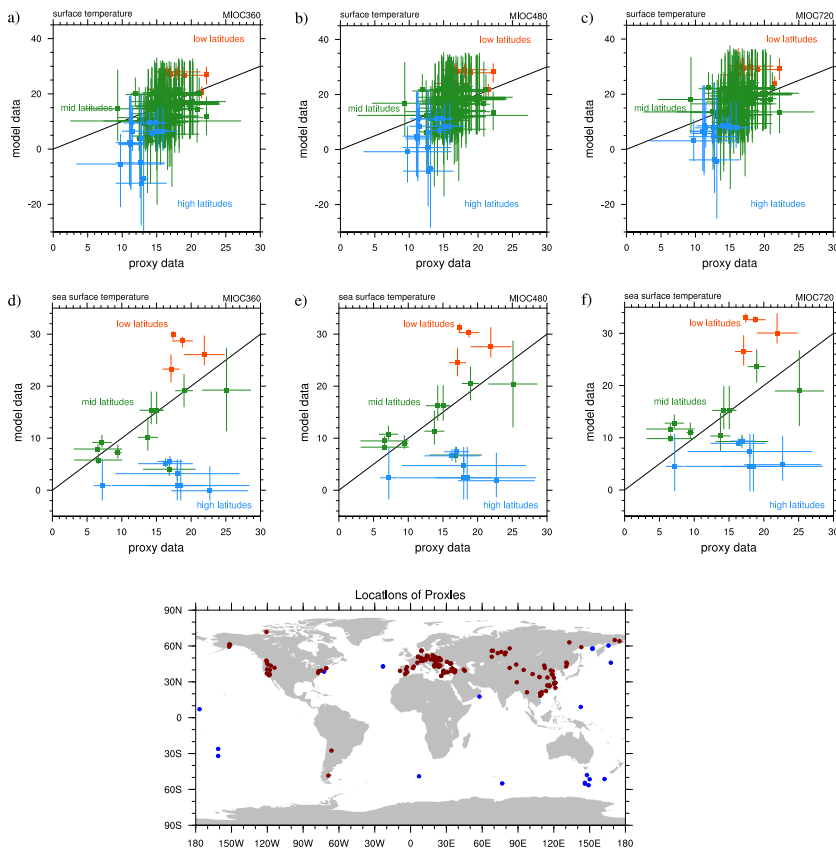


**Fig. 13.** Comparison of model output with (a–c) terrestrial and (d–f) marine temperature reconstructions. The low latitudes are defined to be between the equator and  $30^{\circ}$  N/S, midlatitudes are between  $30$  and  $55^{\circ}$  N/S, and high latitudes are poleward of  $55^{\circ}$  N/S. The location of the proxies is shown in the lower panel.